https://doi.org/10.1016/j.cemconcomp.2023.104998

This is the Pre-Published Version.

Seawater Sea-sand Engineered Geopolymer Composites (EGC) with High Strength and High Ductility

Jian-Cong Lao [1]; Bo-Tao Huang [2] (*); Ling-Yu Xu [3]; Mehran Khan [4];
Yi Fang [5]; Jian-Guo Dai [6] (*)

Highlights

- Seawater Sea-sand EGC (SS-EGC) were developed and investigated for the first time.
- Using seawater and sea-sand slightly decreased the compressive strength of EGC.
- The content of hydrotalcite phases in SS-EGC matrix was higher than that of freshwater EGC.
- Using seawater and sea-sand in EGC increased the tensile strength but lowered the tensile strain capacity.
- The developed SS-EGC showed significantly lower embodied carbon than the cement-based counterpart in the literature.

---

[1] Research Associate, Department of Civil and Environmental Engineering, The Hong Kong Polytechnic University, Hong Kong, China. E-mail: Attic.lao@connect.polyu.hk

[2] Research Fellow, Department of Civil and Environmental Engineering, The Hong Kong Polytechnic University, Hong Kong, China. E-mail: botaohuang@zju.edu.cn (**Corresponding Author*)

[3] Ph.D., Department of Civil and Environmental Engineering, The Hong Kong Polytechnic University, Hong Kong, China. E-mail: ling-yu.xu@connect.polyu.hk

[4] Postdoctoral Fellow, Department of Civil and Environmental Engineering, The Hong Kong Polytechnic University, Hong Kong, China. E-mail: drmehrankhan@outlook.com

[5] Research Associate, Department of Civil and Environmental Engineering, The Hong Kong Polytechnic University, Hong Kong, China. E-mail: yfang20@crimson.ua.edu

[6] Professor, Department of Civil and Environmental Engineering, The Hong Kong Polytechnic University, Hong Kong, China. E-mail: cejgdai@polyu.edu.hk (**Corresponding Author*)

Abstract

In this study, seawater sea-sand Engineered Geopolymer Composites (SS-EGC) were developed and investigated for the first time. The developed EGC achieved high compressive strength (over 140 MPa) and high tensile ductility (around 8%) simultaneously. Emphasis was placed on understanding the influence of seawater and sea-sand (compared to freshwater and washed sea-sand) on the matrix properties and tensile performance of EGC, with two fly ash-to-slag ratios (8:2 and 2:8) considered in the matrices. Results showed that the use of seawater hindered the reaction of EGC matrix and led to a slight reduction of compressive strength (compared to the freshwater counterpart). It was found that the content of hydrotalcite phases in SS-EGC matrix was higher than that of freshwater EGC. In addition, using seawater was found to increase the average modulus of matrix obtained from nanoindentation, leading to a higher fiber/matrix bond strength. The tensile strain capacity of SS-EGC was slightly lower than that of freshwater EGC. The developed SS-EGC showed superior crack resistance and significantly lower embodied carbon than the cement-based counterpart from the literature (with similar compressive strength). The findings of this study provided useful knowledge for the design and development of high-strength high-ductility SS-EGC towards sustainable and resilient marine infrastructures.

Keywords

Engineered Geopolymer Composites (EGC); Strain-Hardening Geopolymer Composites (SHGC); Alkali-activated materials; Seawater; Sea-sand; Low carbon

1 Introduction

In the past three decades, two important advances in concrete technology may be considered, i.e., the design and development of Engineered Cementitious Composites [ECC, also known as Strain-Hardening Cementitious Composites (SHCC)] [1, 2, 3, 4] and Ultra-High-Performance Concrete [UHPC, also known as Reactive Powder Concrete (RPC)] [5, 6, 7, 8]. ECC materials are micromechanically designed to achieve strain-hardening and multiple cracking responses under tensile loadings [9, 10]. The compressive strength and tensile ductility of ordinary ECC are usually 20–80 MPa and 2–10%, respectively. On the other hand, UHPC are featured with ultra-high compressive strength (typically ≥ 150 MPa) and excellent durability, but its tensile ductility is typically below 1%. To achieve high/ultra-high compressive strength and tensile ductility simultaneously in concrete, ECC with high strength (HS, 80–150 MPa) and ultra-high strength (UHS, 150–210 MPa) have been designed and developed in the recent decade [11, 12, 13, 14]. Owing to the superior mechanical performance and dense microstructures, HS/UHS-ECC show promising potential in structural applications under complex/extreme loading and environmental conditions, especially in marine and coastal regions [15, 16, 17, 18].

One of the major concerns for the construction of concrete infrastructure in marine/coastal regions is the shortage of freshwater and river sand on-site [19, 20, 21], which are indispensable raw materials for concrete casting. To address this challenge, seawater sea-sand concrete [also seawater sea-sand ECC (SS-ECC)] reinforced with non-corrosive reinforcements [e.g., fiber-reinforced polymer (FRP) composites] was proposed as an emerging solution, which is promising for sustainable and durable marine/coastal infrastructures [17, 19]. Recently, Huang et al. [23, 24] developed high-strength SS-ECC with a compressive strength of over 130 MPa and tensile ductility of about 5%, and also proposed a probabilistic-based model to describe the crack evolution of SS-ECC. In addition, high-strength SS-ECC reinforced by FRP is a promising approach to developing sustainable structural components with high strength, durability, and ductility. It should be pointed out that although using seawater and sea-sand can improve the greenness of ECC materials, the high-volume cementitious binders used in ECC (especially in HS/UHS-ECC system) [13] still remain a concern for the sustainability issue.

Geopolymer is considered a greener alternative to Portland cement in concrete production [25, 26, 27, 28]. Thus, one emerging technical route to enhance the greenness of the ECC matrix was using a geopolymer-based binder system to replace the Portland cement-based one. In such cases, ECC with geopolymer matrix is named as Engineered Geopolymer Composites [EGC, also known as Strain-Hardening Geopolymer Composites (SHGC)] [29, 30, 31, 32, 33]. Like cement-based ECC, EGC also show significant strain-hardening and multiple cracking behaviors under tension. Most of the existing EGC showed a compressive strength of 30–80 MPa and tensile ductility of 2–8%. Up to now, the highest compressive strength of EGC reported in the literature was 102 MPa, while the corresponding tensile strain capacity was only 1.0% [34]. However, it is still quite challenging to develop EGC materials with both high compressive strength and high tensile ductility.

According to the aforementioned background, the design and development of high-strength high-ductility EGC using seawater and sea-sand is meaningful for constructing high-performance and sustainable marine/coastal structures. On the one hand, using geopolymer matrix in HS-ECC can effectively enhance the material's greenness. On the other hand, the characteristics of high strength and high ductility are beneficial for improving the structural performance of FRP-EGC components. However, up to now, almost no published work could be found on seawater sea-sand EGC (SS-EGC). Developing EGC with high compressive strength (e.g., over 120 MPa) and high tensile ductility (e.g., over 8%) even remains unrevealed for the research community.

This study aims to design and develop SS-EGC with high strength and ductility, and tries to understand the influence of seawater (compared to freshwater) on the matrix properties and tensile performance of EGC. Geopolymer matrices with two different fly ash-to-slag ratios (i.e., 8:2 and 2:8 to respectively represent fly ash-dominated mix and slag-dominated mix) were considered in SS-EGC production. Reaction heat, thermogravimetric analysis (TGA), and nanoindentation were utilized to analyze the properties and microstructures of EGC matrix. Direct tensile performance and cracking behavior were investigated with the help of Digital Image Correlation (DIC) method. Finally, the tensile properties and embodied carbon of the developed SS-EGC and the cement-based SS-ECC in the literature were compared and discussed.

2 Experimental programs

2.1 Raw materials

In this study, sea sand with a maximum size of 1.18 mm was obtained locally from Hong Kong (**Fig. 1**). Artificial seawater was prepared by dissolving commercial sea salt into tap water (with a dosage of 36 g/L), and the tap water in Hong Kong had a salinity lower than 0.1 g/L [19]. It is noted that the commercial sea salt and tap water used in this study were the same with those in the authors' previous studies [17, 23, 24], wherein the chemical composition of the artificial seawater was close to that of the natural seawater along the coasts in Hong Kong as reported in the previous study [23].

The precursors of EGC contained fly ash (FA), ground-granulated blast-furnace slag (GGBS) and silica fume. Their chemical components tested by X-ray fluorescence (XRF) are listed in **Table 1**. FA can be classified as class F according to ASTM C618-19 [35]. The particle size distributions and morphologies can be found in **Fig. 2** and **Fig. 3**, respectively. It can be seen that spherical and angular shape particles were predominant in FA and GGBS, respectively, and SF showed a much smaller particle size.

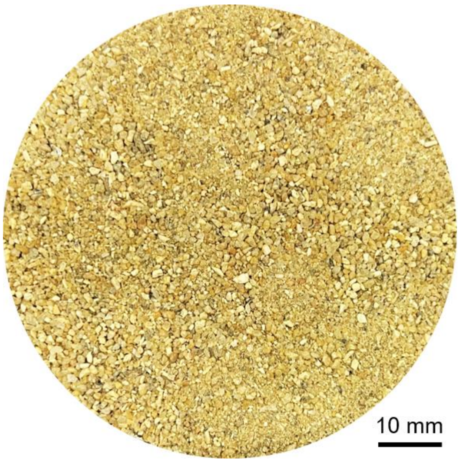

Fig. 1 Photograph of sea-sand with a maximum particle size of 1.18 mm.

Table 1 Chemical components of raw materials (%).

Chemical Composition	FA	GGBS	SF
Aluminum Oxide, Al_2O_3	20.20	12.80	0.15
Silicon Oxide, SiO_2	47.10	29.40	95.20

Calcium Oxide, CaO	8.37	46.60	0.52
Ferric Oxide, Fe_2O_3	14.50	0.36	0.06
Magnesium Oxide, MgO	2.64	7.47	1.08
Sulfur Trioxide, SO_3	0.79	1.67	0.12
Titanium Dioxide, TiO_2	2.04	0.80	/
Phosphorus Oxide, P_2O_5	0.80	0.11	0.32
Potassium Oxide, K_2O	2.1	0.40	0.77
Others	0.66	0.19	0.03
LOI (950 °C)	0.80	0.20	1.75

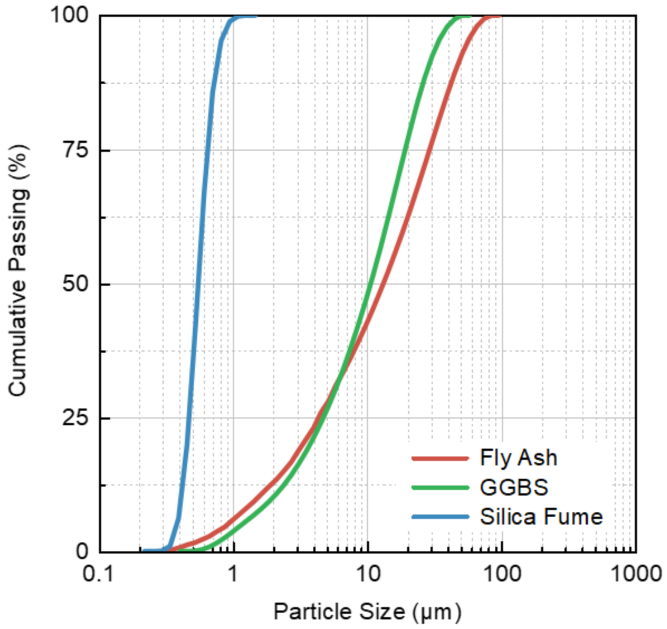

Fig. 2 Particle size distributions of raw materials.

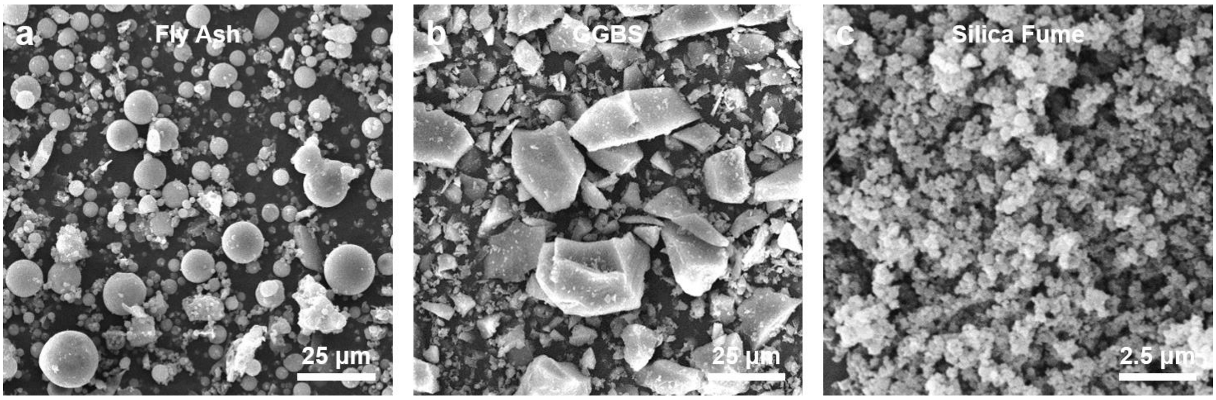

Fig. 3 SEM images of (a) fly ash, (b) GGBS, and (c) silica fume.

Sodium metasilicate anhydrous (in solid) and waterglass (in liquid) were used as alkali activators to produce the EGC matrix. Analytical-grade sodium metasilicate anhydrous in powder form was composed of 50.5% Na_2O and 47.2% SiO_2 in weight (SiO_2 / Na_2O = 0.94). Waterglass had 8.7% Na_2O, 27.7% SiO_2, and 56.8% H_2O in weight (SiO_2 / Na_2O = 3.18). Additionally, analytical-grade borax ($Na_2B_4O_7 \cdot 10H_2O$) with 99.5% purification was employed as a retarder.

Fiber reinforcements used in EGC were 18 mm-length ultra-high-molecular-weight polyethylene (PE) fibers, with a diameter of 24 μm. The mechanical properties provided by the manufacturer (Beijing Quantumeta AMT Co. Ltd) were as follows: 1) Strength: 3000 MPa, 2) elastic modulus: 100 GPa, and 3) density: 0.97 g/cm^3.

2.2 Preparations of EGC and SS-EGC

Fly ash and GGBS are the mostly used precursors for geopolymer. Alkali-activated fly ash alone always has setting issue, known as a long setting time and a slow strength development at ambient environment following. Whereas, alkali-activated GGBS alone, on the contrary, exhibits fast setting and high early strength. Blending fly ash and GGBS is now a popular way to produced geopolymer. It has also been demonstrated in Ref. [CCR] that using fly ash/GGBS ratio of 8:2 and 2:8 guaranteed satisfactory mechanical properties and didn't have setting issue (too fast or too slow), which will also be used in this study. On this basis, the effect of seawater and sea sand were considered as another variable. Finally, the mix proportions of EGC and SS-EGC are given in **Table 2**. The differences between the mixes were FA/GGBS ratios (i.e., 8:2 and 2:8), types of sand (i.e., sea-sand and washed sea-sand), types of water (i.e., seawater and freshwater), while other factors remained the same. The mix IDs are shown in the form of "F*a*S*b*-*c*", wherein F and S denote FA and GGBS, respectively. *a/b* denotes two FA/GGBS ratios (in mass), and *c* denotes freshwater (F) or seawater (S). Seawater and sea-sand were used for SS-EGC (i.e., F8S2-S and F2S8-S in **Table 2**). For the other two control groups (i.e., F8S2-F and F2S8-F in **Table 2**), freshwater and freshwater-washed sea-sand were used. It is noted that the tensile performance of ECC/EGC materials is sensitive to the sand properties. Thus, freshwater-washed sea-sand was used in the control groups to minimize the influence of other properties of the sand.

Table 2 Mix proportions of EGC and SS-EGC (weight ratio).

Mix IDs	Precursors (Total 1.000)			Borax	Activators		Extra Water	Total Water	Sand	PE Fibers
	FA	GGBS	SF		Na_2SiO_3-Anhydrous	Waterglass				
F8S2-F	0.760	0.190	0.050	0.038 (Water of Crystallization: 0.018)	0.095	0.141 (Water Content: 0.080)	0.152 (FW)	0.250	0.300 (WS)	2.0 (Vol. %)
F8S2-S	0.760	0.190					0.152 (SW)		0.300 (SS)	
F2S8-F	0.190	0.760					0.152 (FW)		0.300 (WS)	
F2S8-S	0.190	0.760					0.152 (SW)		0.300 (SS)	

Note: WS (Washed Sand), SS (Sea-Sand), FW (Freshwater), and SW (Seawater).

For all the mixes, the water (the sum of extra water, water in waterglass, and crystal water in borax)-to-precursor ratios were the same (i.e., 0.250). The low water/precursors ratio used in this study could induce an alkali solution with a high PH value, which could cause rapid setting during the preparation of samples. Borax ($Na_2B_4O_7 \cdot 10H_2O$) was used as a retarder to avoid flash setting during the preparation of samples. Sand-to-precursor ratio was chosen as 0.3, which has been widely used in strain-hardening cement-based materials. Sodium metasilicate and waterglass were used in combination with a Na_2O-to-precursor ratio of 6.5% and a SiO_2-to-Na_2O ratio of 1.3. 18-mm PE fibers (2 Vol.%) were used as the fiber reinforcement.

During the EGC preparation, activators, borax, and extra water (artificial seawater or freshwater) were first mixed together. Precursors were weighted and dry-mixed for 5 min, followed by adding the prepared alkali solution and mixing for another 10 min until a uniform slurry formed. PE fibers were then added to the slurry and mixed for 5 min before casting. The specimens were demolded after 24 h ambient curing and wrapped with plastic film to avoid excessive moisture loss. Finally, the specimens were placed at ambient temperature in the laboratory (23 °C) until 28 d.

2.3 Testing methods

The compressive strength was measured by a 50-mm cube following ASTM C109/C109M [36]. The loading rate was 1.0 MPa/s, and three identical cubes were tested for each mix. Direct tensile test was performed by three dog-bone shape specimens for each group (**Fig. 4**) following

JSCE recommendations [37], with a displacement-control loading rate of 0.5 mm/min. The wider side of the specimens was sprayed with a speckle pattern for Digital Image Correlation (DIC) analysis. During the test, the photographs of the speckled side were captured continuously by a digital camera at an interval of 3 s. Two linear variable differential transformers (LVDTs) were set symmetrically to measure the deformation of the 80-mm length central area.

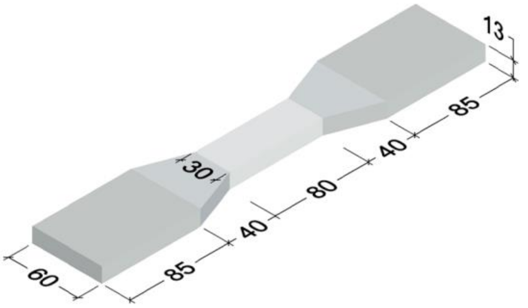

Fig. 4 Dimensions of dumbbell sample for the direct tensile test (unit: mm).

The evolution of reaction heat of the geopolymer matrix was recorded by an isothermal calorimeter (Calmetrix I-Cal 4000) to investigate the effect of seawater on the early-age reaction process. Before the test, the alkali solution and all the solid materials (without sands and fibers) were maintained at 20 °C in a temperature-conditioned room for 24 h. Then, external mixing was performed for 3 min to ensure the homogeneity of the matrix. It is noted that the very early reaction heat during the external mixing could not be captured. Following that, the slurry was put into the isothermal calorimeter for 72-h testing at 20 °C.

For the following tests, paste samples were prepared, excluding fibers and sand. Thermogravimetric analysis (TGA) was employed to quantify the reaction product. Powder with a particle size smaller than 75 μm was prepared and subjected to freeze drying for 72 h at -84 °C. During the TGA test (Rigaku, Thermo Plus EVO2), the samples were stabilized at 60 °C for 30 min, and then heated to 900 °C at a rate of 10 °C/min in an atmosphere with nitrogen flowing (20 ml/min). Fragments cut from the inner region of the paste were used for nanoindentation tests. These fragments were then fixed in epoxy and polished to obtain a smooth surface. For the nanoindentation (Bruker's TI Premier TriboIndenter), each indentation was done over an 11 × 11 grid (100 μm × 100 μm), with a gap between adjacent points of 10 µm. The loading protocol followed [5 s loading – 2 s holding in the peak load (2000 µN) – 5 s unloading] in a linear manner.

3 Compressive strength and matrix characteristics

3.1 Compressive strength

Fig. 5 compares the 28-d compressive strengths of EGC. Generally, the mixtures showed high compressive strengths over 80 MPa. For the freshwater mixes, F8S2-F and F2S8-F gained a compressive strength of 89.0 MPa and 145.1 MPa, respectively. As confirmed in [CCR], mixtures with higher content of GGBS can generate the reaction product (mainly C-(N)-A-S-H) of higher Ca/Si ratio with enhanced space-filling effect [38], which subsequently reduced the porosity caused by unbound water and densified the microstructure, finally increased the strength.

SS-EGC exhibited marginal decreases in 28-d compressive strength as compared to their freshwater counterparts, and the reduction in F8S2 (-5.0%) was more pronounced than that in F2S8 (-1.5%). This deterioration of compressive strength may be related to the interaction between seawater and alkali activator [see **Eq. (1)**] during the preparation of seawater-mixed sodium silicate solution as revealed by Shi et al. [39]. $MgCl_2$ in seawater could react with sodium silicate and consequently form magnesium silicate hydrate (M-S-H) gels and amorphous SiO_2. This reaction unavoidably decreased the alkali and soluble silica contents in the alkali-activator solution. It was reported that lower alkali content would post a severer degradation on FA-dominant mixtures than GGBS-dominant mixtures [40], which could explain the difference between the compressive strength degradations of F2S8 and F8S2 series. In addition, the nano-size M-S-H gel would also attach on the unreacted particles, which further impeded the dissolution of the precursors [39, 41].

(1)

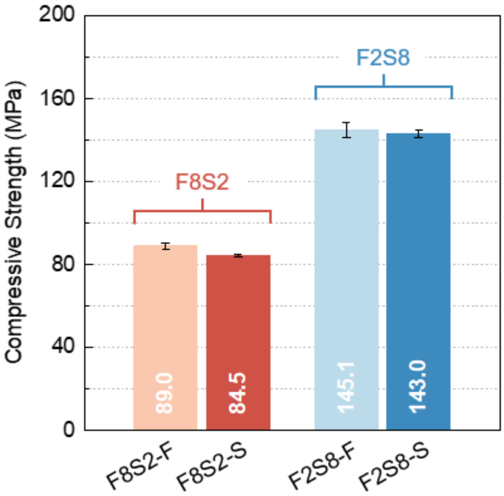

Fig. 5 Compressive strength of EGC. Using seawater and sea-sand slightly decreased the compressive strength of EGC for both F8S2 and F2S8 series.

3.2 Reaction heat

The reaction heat release rate and cumulative heat of the alkali-activating reaction were plotted together in **Fig. 6**. For F2S8 series, the heat evolution followed Type III Model proposed by Shi and Day [42], which contained five stages as: 1) initial and additional initial peaks, 2) induction period, 3) acceleration period, 4) deceleration period, and 5) steady-state diffusion stage. Due to the external mixing process, this study did not record the initial stage corresponding to the first peak in the first few minutes. This peak was attributed to the wetting and initial dissolution of precursors. In the plotted curves, the different initial stage displayed as the second peaks, which correspond to the reaction between dissolved cations (e.g., Ca^{2+} and Na^{2+}) and anion/anions group (e.g., $[SiO_4]^{4-}$) from activators to form the primary reaction product [42]. It can be seen from **Fig. 6** that seawater significantly lowered the additional initial peak because the seawater alkali-activator had a lower soluble silica content as a reactant to form a primary hydration product. Consequently, the acceleration and deceleration stages corresponding to the precipitation of reaction products were retarded and alleviated by seawater subsequently. Finally, almost no difference was shown in the steady-state diffusion stage between freshwater and seawater mixes.

For F8S2 series, the phenomenon was similar, with a lower heat releasing rate and an absent acceleration and deceleration period. This was related to the longer geopolymerization period of alkali-activated FA as a result of its low reactivity. But it is still evident that the additional initial period in F8S2 was also hindered by seawater. Although the heat release was apparently changed with seawater, the cumulative heat was only slightly lower, indicating a slightly lower degree of reaction.

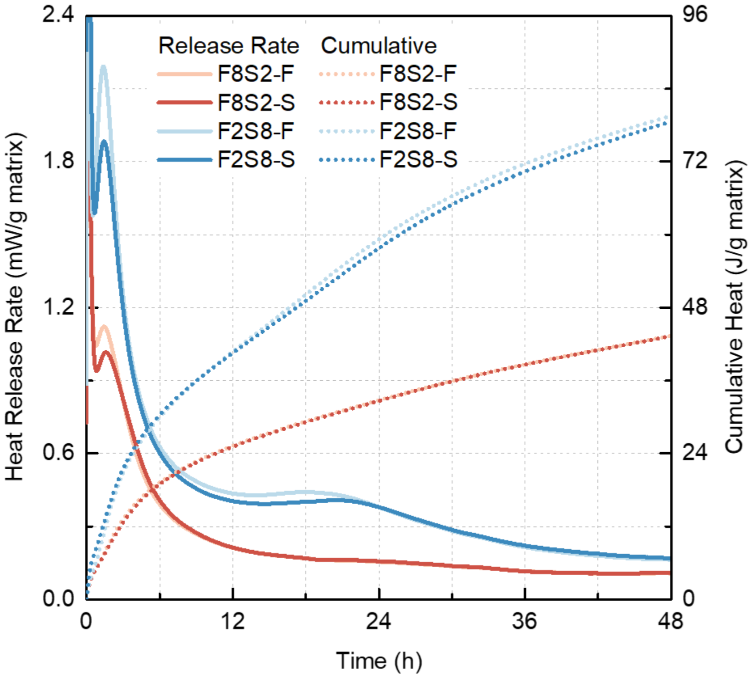

Fig. 6 Reaction heat of EGC and SS-EGC. SS-EGC mixes showed slightly lower heat releasing rate compared to the freshwater counterpart.

3.3 TGA analysis

Fig. 7 shows the thermogravimetric (TG) and differential thermogravimetric (DTG) curves of EGC and SS-EGC. Referring to the DTG curves, the weight loss below 200ºC attributed to the decomposition of sodium-substituted calcium aluminosilicate hydrate [C-(N)-A-S-H], which was the main product to support strength of EGC and SS-EGC [43, 44] and contributed to the most significant mass loss in all the mixtures. It was also reported that in seawater-mixed alkali-activated materials, aluminium chloride hydrate might exist and decompose within 200–400ºC [45]. Accordingly, the hydrotalcite phase contributed to the secondary peak at 400ºC, which might contain CO_3-hydrotalcite (420ºC) [46] or Cl-hydrotalcite in the presence of seawater (400ºC) [47]. The decomposition of low-crystalline calcite caused the small hump centered at 508ºC. After that, the residual peaks could be carbonates [i.e., calcite within 600–800ºC and $CaMg(CO_3)_2$ within 550–750ºC [48]], and further decompositions of C-A-S-H to wollastonite (800ºC) and mayenite (600–950ºC) [49, 50].

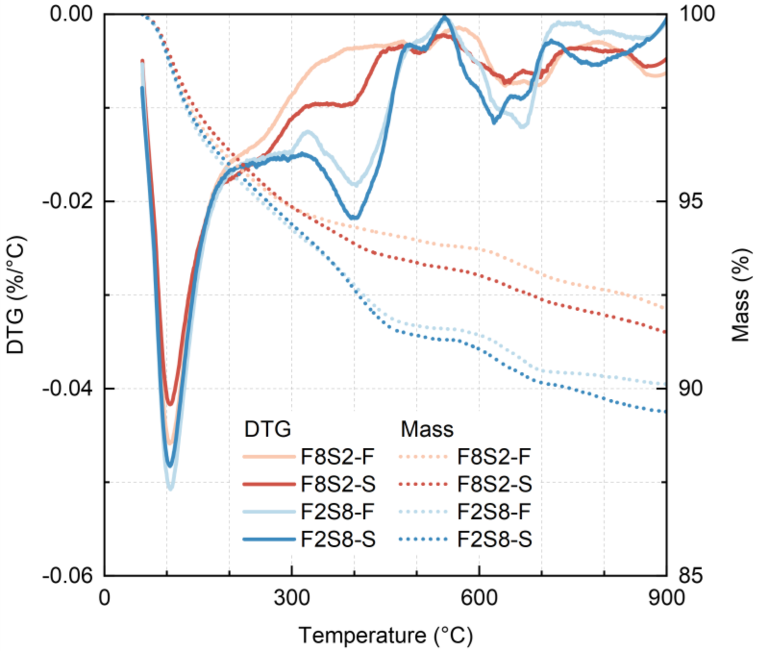

Fig. 7 TG and DTG curves of EGC and SS-EGC. The influence of seawater on the TG curves of F8S2 series was more prominent than that of F2S8 series.

For both F8S2 and F2S8, incorporating seawater would reduce the C-(N)-A-S-H content due to the lower degree of reaction (caused by the interaction between seawater and alkali activator), which is associated with the slight reduction of compressive strength. On the contrary, the hydrotalcite contents detected at around 400ºC were higher in the seawater mixtures. The Mg^{2+} and Cl^- in seawater might have provided additional sources for forming the Cl-hydrotalcite phase in the reaction product, thus enriching the total hydrotalcite phase in the reaction product. It can also be seen that F8S2-S tended to show higher mass loss within 200-400ºC than F8S2-F, which indicates the formation of aluminium chloride hydrate in F8S2-S. In comparison, a less significant difference was observed between F2S8-F and F2S8-S due to the lower Al source of precursors (i.e., FA had a higher Al content than GGBS).

3.4 Nanoindentation

Before performing nanoindentation tests, the surface roughness of the well-polished samples was tested by scanning probe microscopy on a 40 × 40 μm^2 area. As shown in **Fig. 8**, the root-mean-square roughness (R_q) was 23.8 nm, indicating that the surface was flat enough for a reliable test result [51].

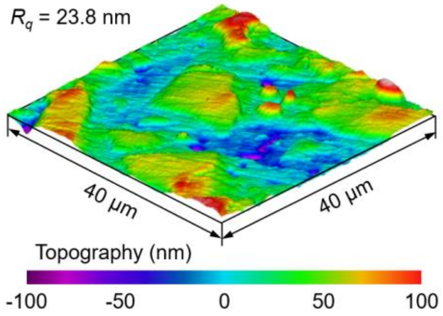

Fig. 8 Surface roughness of the nanoindentation samples tested by scanning probe microscopy (R_q = 23.8nm).

During the test, the loading protocol with a maximum load of 2000 μN resulted in a series of nanoindentation responses in the form of a load-indentation depth relationship. **Fig. 9** shows the typical nanoindentation responses of each phase extracted from F2S8-F, wherein low-density (LD) C-(N)-A-S-H, high-density (HD) C-(N)-A-S-H, ultra-high-density (UHD) phase, unreacted FA, and unreacted GGBS were presented. Given all these curves, the unloading segment was used to calculate the reduced modulus E_r. Then, the E_r value of each indent was converted to elastic modulus (E) by Oliver and Pharr method [52] by assuming the Poisson ratio as 0.2. Finally, statistic deconvolution based on Gauss mixture model was performed to gain the micromechanical properties, and the fraction of each phase was evaluated, according to the same method reported by Fang et al. [53]. For each mix, 484 points (22 × 22) were used for analysis.

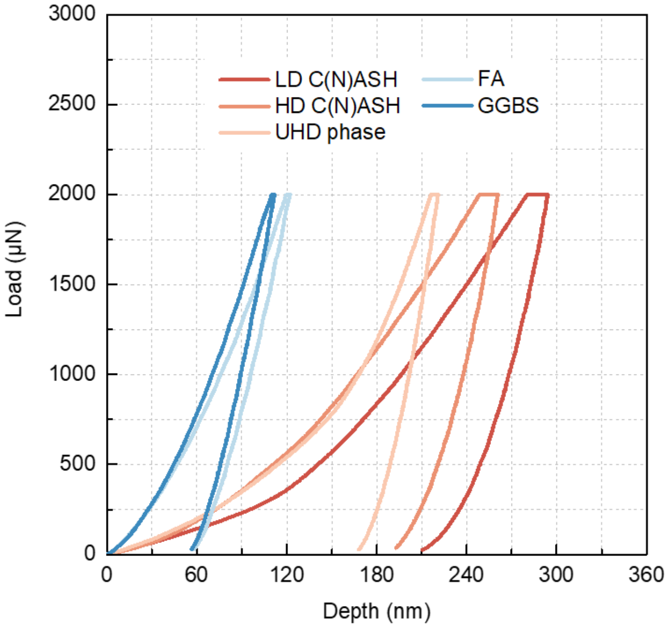

Fig. 9 Typical load-indentation depth curve for each phase in the matrix.

Table 3 and **Fig. 10** display the deconvolution results of nanoindentation. Regarding the elastic modulus, C-(N)-A-S-H and UHD phase showed higher values in the case of F2S8 series than F8S2 series. This was related to different gel structures and chemical assemblages formed by different FA/GGBS ratios [38]. It has been revealed in [CCR] that the C-(N)-A-S-H gel and UHD phase of higher density and higher Calcium content were preferentially formed in F2S8 relative to F8S2 due to the higher GGBS content in the former, which showed a superior nanoindentation response.

Table 3 Average elastic modulus (*E*) of single phases after deconvolution (Unit: GPa)

Mix IDs	LD C(N)ASH	HD C(N)ASH	UHD Phase	Unreacted FA	Unreacted GGBS
F8S2-F	22.64±3.67 (36%)	29.25±5.64 (30%)	43.20±8.28 (15%)	70.02±12.54 (15%)	95.53±8.05 (4%)
F8S2-S	21.96±2.96 (32%)	29.39±4.49 (28%)	42.52±4.52 (18%)	67.21±12.92 (16%)	96.34±9.56 (6%)
F2S8-F	26.90±3.25 (33%)	32.58±5.21 (24%)	47.95±8.79 (17%)	71.80±5.25 (9%)	89.01±5.51 (17%)
F2S8-S	26.38±2.30 (27%)	34.63±3.94 (21%)	47.03±8.78 (20%)	72.34±7.98 (9%)	96.94±9.23 (23%)

Note: The value in parentheses denotes the fraction of the corresponding phase.

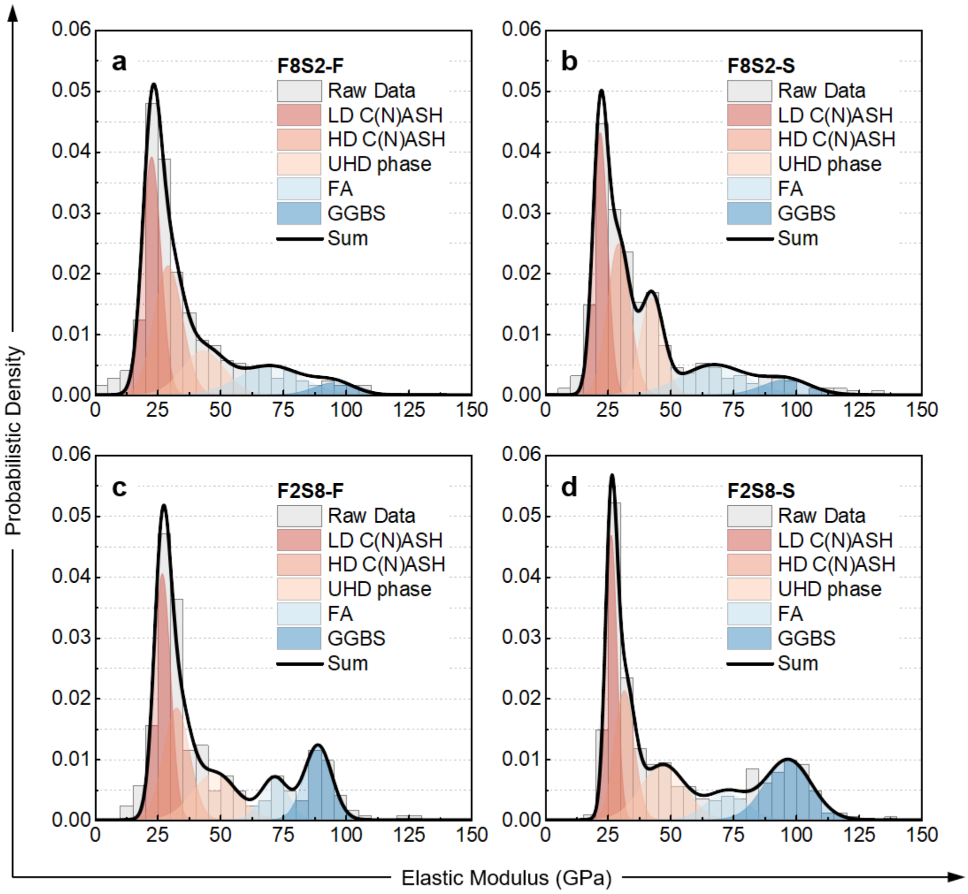

Fig. 10 Distribution of the elastic moduli of different phases in matrix. The elastic modulus of each phase was not changed with the use of seawater.

From **Table 3**, it can be found that using seawater in the mixture did not significantly change the average elastic modulus of each phase. However, the fraction of each phase altered when seawater was added, as summarized in **Table 3** and **Fig. 11**. Obviously, the fractions of LD and HD C-(N)-A-S-H decreased in the seawater mixes compared to the freshwater counterparts. Specifically, the fraction of LD and HD C-(N)-A-S-H decreased by 10% for F8S2-S and 16% for F2S8-S, while the unreacted particles increased. This should be because of the lower degree of reaction in the seawater mixes, as aforementioned in ***Section 3.1*** and ***Section 3.2***. Interestingly, the UHD phases with an elastic modulus around 45 GPa increased to some extent in SS-EGC (20% and 17% increase for F8S2 and F2S8, respectively). As depicted in Zhang et al. [54], the hydrotalcite phase roughly has a modulus higher than 40 GPa, and Moradi et al. [55] regarded the phase in a sample of alkali-activated slag with a modulus around 45 GPa as C-S-H with hydrotalcite nanocrystals. Therefore, UHD phase in this study might consist of the intermix of C-(N)-A-S-H and hydrotalcite nanocrystals. As confirmed in TGA, hydrotalcite phases increased in F8S2-S and F2S8-S compared to their freshwater counterparts, which was consistent with the fraction increase of the UHD phase in nanoindentation. This observation provides further evidence for the presence of hydrotalcite in the UHD phase in alkali-activated FA and GGBS.

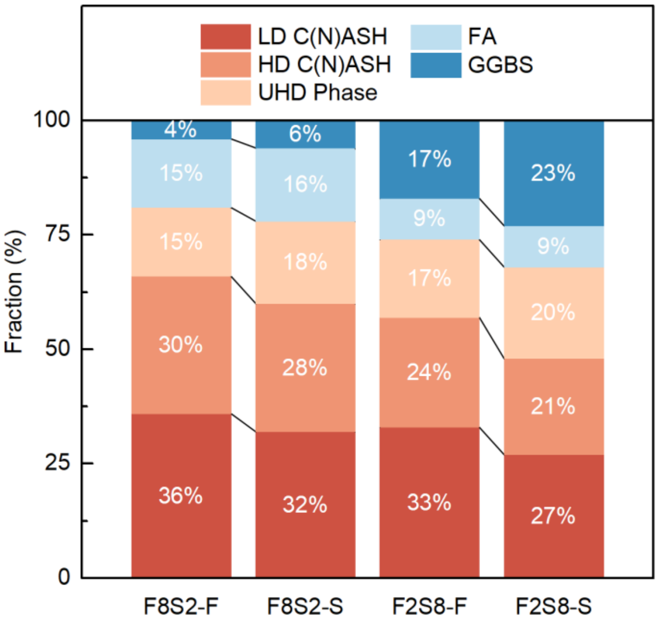

Fig. 11 Fraction of each phase in matrix. For both F8S2 and F2S8 series, the use of seawater increased the fraction of UHD phase but decreased the fractions of LD and HD C-(N)-A-S-H.

4 Tensile performance and cracking behavior

4.1 Tensile performance

The tensile stress–strain curves of EGC and SS-EGC are presented in **Fig. 12**, and the averaged curve of each group is also plotted for comparison. The obtained tensile strengths and strain capacities are summarized in **Table 4**. Significant tensile strain-hardening behavior can be observed for all the mixes studied, and the tensile strain capacities of F8S2-F, F8S2-S, F2S8-F, and F2S8-S were 8.7%, 8.1%, 8.6%, and 6.9%, respectively. It can be found that using seawater and sea-sand decreased the tensile ductility of EGC and the reduction was more significant for the F2S8 series. The tensile strengths of the F2S8 series were higher than those of the F8S2 series, and the use of seawater and sea-sand increased the tensile strengths of both series (see **Fig. 12c** and **Fig. 12f**).

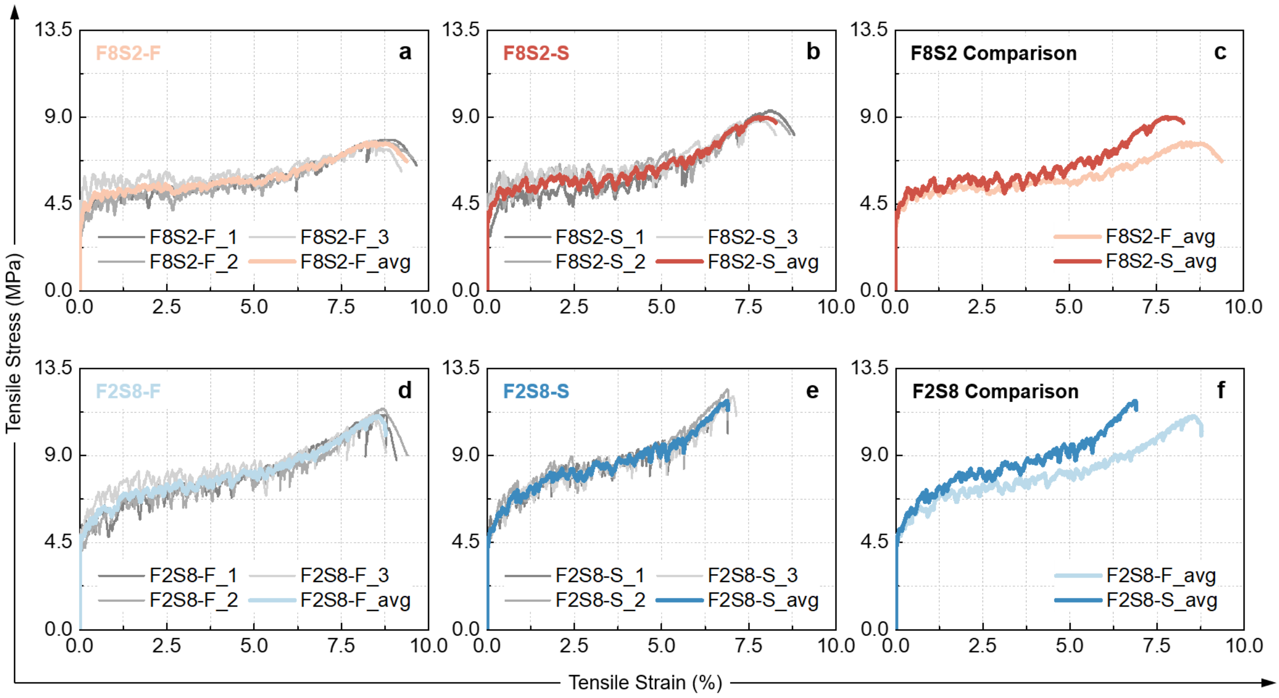

Fig. 12 Tensile stress–strain curves of EGC and SS-EGC. Using seawater and sea-sand increased the tensile strength but decreased the tensile ductility.

Table 4 Summary of mechanical properties EGC and SS-EGC.

Mechanical Properties	F8S2		F2S8		Cement-based SS-ECC [24]
	F8S2-F	F8S2-S	F2S8-F	F2S8-S	
Compressive Strength (MPa)	89.0	84.5	145.1	143.0	134.0
Tensile Strain Capacity (%)	8.7	8.1	8.6	6.9	7.1
Tensile Strength (MPa)	8.1	9.0	11.2	11.9	7.1
Average Crack Width, w_{Avg} (μm)	63.5	62.4	70.0	59.4	86.0
$1/w_{\mathrm{Avg}}$ (1/μm)	0.016	0.016	0.014	0.017	0.012
Crack Width Deviation, s_w (μm)	19.1	21.8	23.4	15.7	45.6
$1/s_w$ (1/μm)	0.052	0.046	0.043	0.064	0.022

As reported in ***Section 3.1***, the compressive strength of EGC slightly decreased when seawater and sea-sand were used to replace the freshwater and washed sand. However, the tensile strength of EGC in **Fig. 12** showed a different trend. It is known that the tensile strength of strain-hardening concrete materials is highly dependent on the fiber interfacial frictional bond [56, 57], and the matrix elastic modulus is important for the fiber/matrix bond [58]. Sonat et al. [59] reported that there was a relationship between fiber/matrix bond and matrix elastic modulus obtained from nanoindentation. Recently, a linear relationship between maximum fiber bridging force and the average elastic modulus of the matrix had been validated [CCR], which provided a linkage between micromechanical properties of the matrix and the maximum tensile strength. Hence, the tensile strength of EGC was plotted together with the average elastic modulus of EGC matrix obtained from nanoindentation (**Fig. 13**). A positive relationship can be observed between the tensile strength and the average modulus of the matrix. In **Fig. 13**, the average moduli of F8S2 matrices were lower than those of F2S8 matrices. In addition, using seawater to replace freshwater increased the average moduli of EGC matrices, leading to a higher tensile strength.

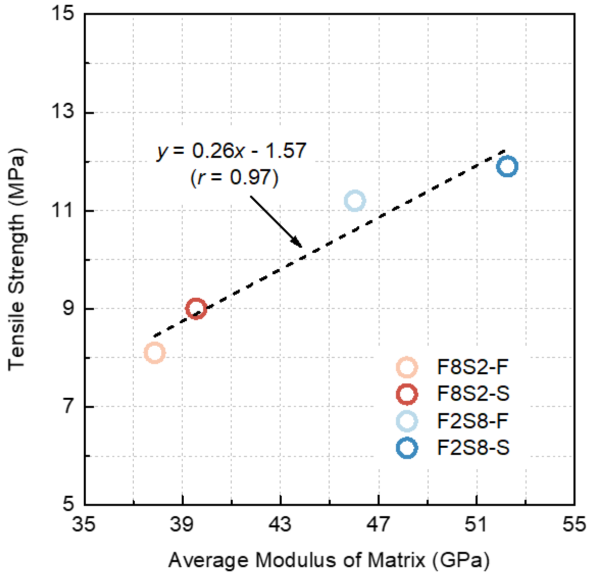

Fig. 13 Relationships between tensile strength and average matrix modulus obtained from nanoindentation. A positive relationship can be observed between these two parameters.

4.2 Cracking behavior

During the direct tensile test of EGC and SS-EGC, digital photographs were taken for DIC analysis. This method has been widely used in monitoring the cracking behavior of strain-hardening concrete materials. **Fig. 14** presents the DIC strain field at the ultimate tensile strain of the EGC and SS-EGC studied, and significant multiple cracking behavior can be observed for all the mixes. Based on the digital image taken at the ultimate tensile strain, the width of each crack at the central area (i.e., 80-mm length area in **Fig. 4**) was measured using the method mentioned in [28]. The average crack width and crack width deviation are also summarized in **Table 4**. Using seawater and sea-sand had a marginal effect on the cracking behavior of the F8S2 series, while decreasing the crack width (from 70.0 to 59.4 μm) and its deviation (from

23.4 to 15.7 μm) of the F2S8 series. For strain-hardening concrete materials, finer crack width could be beneficial to the self-healing behavior.

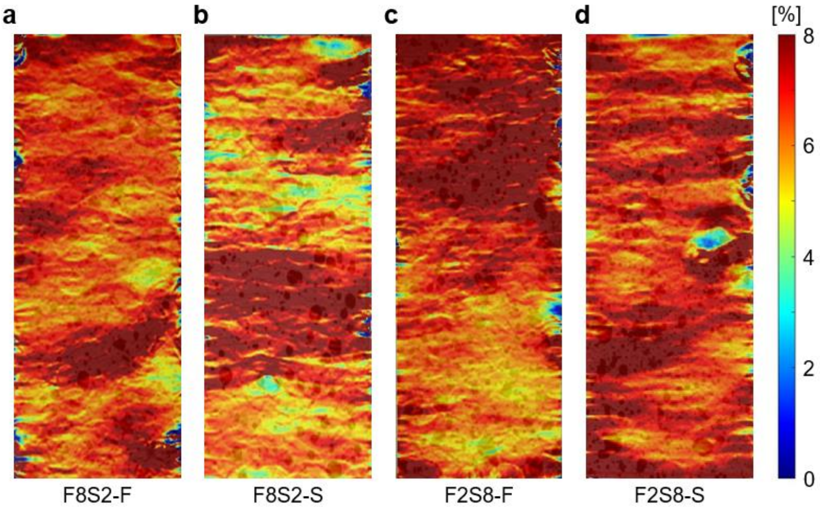

Fig. 14 DIC strain field at the ultimate tensile strain of EGC and SS-EGC. Significant multiple cracking behavior can be observed for all the mixes.

4.3 Assessment of overall performance

To assess and compare the overall performance of EGC and SS-EGC, the five-dimensional assessment of the mechanical properties (i.e., compressive strength, tensile strain capacity, and tensile strength) and cracking behavior (i.e., crack width and crack width deviation at the ultimate tensile strain) were utilized, which was proposed for strain-hardening concrete materials [28]. **Fig. 15** compares the results of the five-dimensional assessment of EGC and SS-EGC. It is noted that smaller crack width and crack width deviation represent better durability and a more stable multiple-cracking process. Hence, the reciprocals of these two parameters are used in **Fig. 15** to achieve a positive correlation between the parameters and performances. For both F8S2 and F2S8 series, the values of the seawater sea-sand group were normalized by the corresponding values of the control group. It can be found in **Fig. 15a** that compared to F8S2, the use of seawater and sea-sand had a more pronounced effect on the properties of the F2S8 series. However, for the F2S8 series in **Fig. 15b**, SS-EGC exhibited lower tensile strain capacity but better crack resistance (i.e., smaller crack width and width deviation).

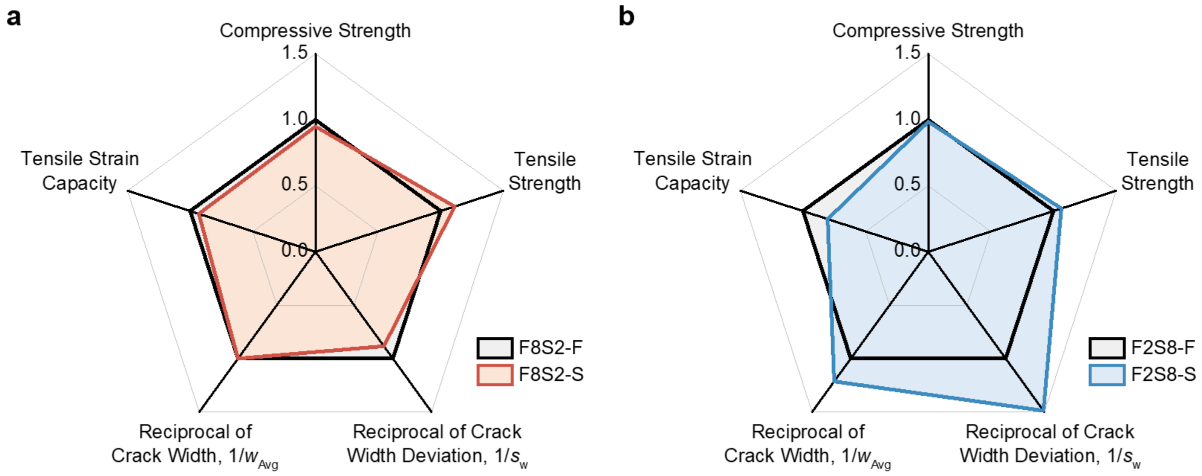

Fig. 15 Five-dimensional assessment of the mechanical properties and cracking behavior of EGC: (a) F8S2 and (b) F2S8 series. Compared to F8S2 series, using seawater and sea-sand had a more pronounced effect on the properties of F2S8 series.

5 Comparison to cement-based SS-ECC in literature

5.1 Comparison of tensile performance

As mentioned in the ***Introduction*** section, the authors previously developed the cement-based SS-ECC with a compressive strength of over 130 MPa [23, 24]. One of the developed SS-ECC in Ref. [24] (Specimen ID: L18-V2.0-S1) was also reinforced by 2% 18-mm PE fibers, which were the same as that used in this study. Also, the compressive strength of L18-V2.0-S1 (134.0 MPa) was close to that of F2S8-S (143.0 MPa). Thus, it is feasible to compare the tensile performance and carbon emission of the aforementioned cement-based SS-ECC and SS-EGC, which can present the differences between these two types of seawater sea-sand concrete. **Table 4** summarizes the mechanical properties of L18-V2.0-S1 reported in Ref. [24].

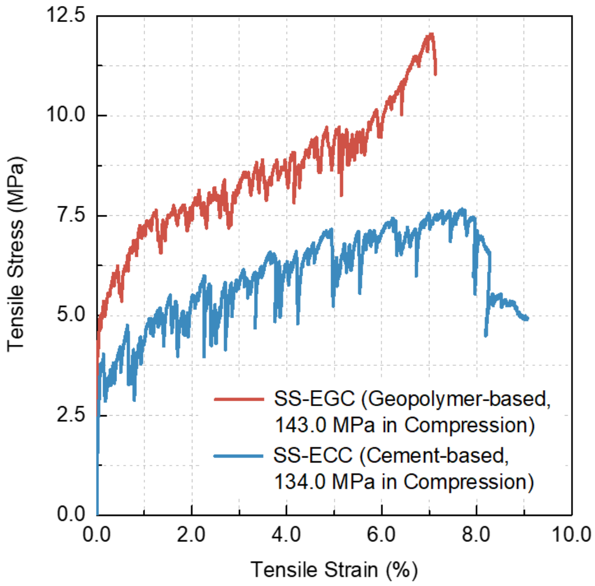

Fig. 16 Comparison of the tensile performance of geopolymer-based SS-EGC (F2S8-S in this study) and cement-based SS-ECC (L18-V2.0-S1 in Ref. [24]) with similar compressive strength. Geopolymer-based SS-EGC showed higher tensile strength and smaller tensile stress fluctuations during the strain-hardening process.

The tensile performance of geopolymer-based SS-EGC (i.e., F2S8-S in this study) and cement-based SS-ECC (i.e., L18-V2.0-S1 in Ref. [24]) are compared in **Fig. 16**, and one typical curve close to the averaged tensile performance of each material was selected and plotted. It is noted that although the tensile performance of ECC materials varied for different mix proportions, the selected SS-ECC was the only one found in the literature with similar compressive strength and the same fiber reinforcement. As summarized in **Table 4**, the tensile strain capacity of SS-EGC (i.e., 6.9%) was close to that of cement-based SS-ECC (i.e., 7.1%), and SS-EGC showed higher tensile strength (also see in **Fig. 16**). It can be found that geopolymer-based SS-EGC showed smaller tensile stress fluctuations during the strain-hardening process (**Fig. 16**), which indicated a finer crack width of SS-ECC in tension (compared to cement-based SS-ECC) [60]. Thus, as presented in **Table 4**, the crack with and crack width deviation of SS-EGC were significantly smaller than those of cement-based SS-ECC. Overall, it could be concluded that the developed SS-EGC had superior tensile performance and crack resistance than the cement-based SS-ECC with similar compressive strength in literature [24]. As the existing data of high-strength SS-EGC and SS-ECC (cement-based) is still limited, further studies are essential to understand the differences between the mechanical properties and cracking behaviors of these emerging materials.

5.2 Comparison of embodied carbon

Table 6 presents the unit embodied carbon, embodied energy, and cost of the raw material used for calculation. The calculated embodied carbon, embodied energy, and cost of SS-EGC and cement-based SS-ECC with similar compressive strength are summarized in **Table 6** and **Fig. 17**. It is mentioned that the embodied carbon of seawater and sea-sand was assumed as zero, as no relevant literature was found. The embodied carbon of waterglass was calculated as the sum of sodium silicate and water. In addition, the embodied carbon of borax was considered as that of the retarder reported in the literature [62].

Table 5 Embodied carbon, embodied energy and cost of raw materials

Raw Materials	Embodied Carbon [(metric ton CO_2)/metric ton]	Embodied Energy (GJ/metric ton)	Cost (HKD/metric ton)
Cement	0.912 [62]	5.5 [65]	800 [69]
FA	0.004 [62]	0.1 [65]	350 [69]
GGBS	0.042 [62]	0.2 [66]	500 [69]
SF	0.024 [63]	0.1 [65]	2100 [69]
Na_2SiO_3	1.860 [26]	9.4 [66]	860 [69]
Waterglass[1]	0.804 [26]	4.07 [66]	2266 [70]
Borax[2]	1.310 [62]	0.82 [67]	7440 [CCR]
Superplasticizer	1.880 [62]	11.47 [65]	60000 [69]
PE Fibers	2.000 [64]	94.5 [68]	200000 [CCR]
Sea-sand[3]	0.000	0	0
Seawater[3]	0.000	0	0

Table 6 Embodied carbon, embodied energy, and cost of SS-EGC and cement-based SS-ECC.

Raw materials	Embodied Carbon (kg CO_2/m^3)		Embodied Energy (MJ/m^3)		Cost (HKD)	
	F2S8-S	SS-ECC [24]	F2S8-S	SS-ECC [24]	F2S8-S	SS-ECC [24]
Cement	/	1119.0 (92.9%)	/	6748.5 (76.3%)	/	981.6 (14.5%)
FA	0.9 (0.2%)	/	23.4 (0.6%)	/	82.0 (1.5%)	/
GGBS	39.4 (7.9%)	/	187.5 (4.8%)	/	468.8 (8.7%)	/
SF	1.5 (0.3%)	7.4 (0.6%)	6.2 (0.2%)	30.7 (0.3%)	129.6 (2.4%)	644.7 (9.6%)

Na_2SiO_3	217.8 (43.6%)	/	1100.7 (28.2%)	/	100.7 (1.9%)	/
Waterglass[1]	140.3 (28.1%)	/	710.2 (18.2%)	/	395.4 (7.3%)	/
Borax[2]	61.3 (12.3%)	/	38.4 (1.0%)	/	348.2 (6.4%)	/
Superplasticizer	/	38.9 (3.2%)	/	237.4 (2.7%)	/	1242.0 (18.4%)
PE Fibers	38.8 (7.8%)	38.8 (3.2%)	1833.3 (47.0%)	1833.3 (20.7%)	3880.0 (71.8%)	3880.0 (57.5%)
Sea-sand[3]	0					
Seawater[3]	0					
Total	500 (100%)	1204.1 (100%)	3899.8 (100%)	8849.9 (100%)	5404.7 (100%)	6748.3 (100%)

[1] Waterglass contains 56.8% H_2O in weight.

[2] Borax includes crystalized water (i.e., $Na_2B_4O_7 \cdot 10H_2O$).

[3] The embodied carbon of seawater and sea-sand was assumed as zero.

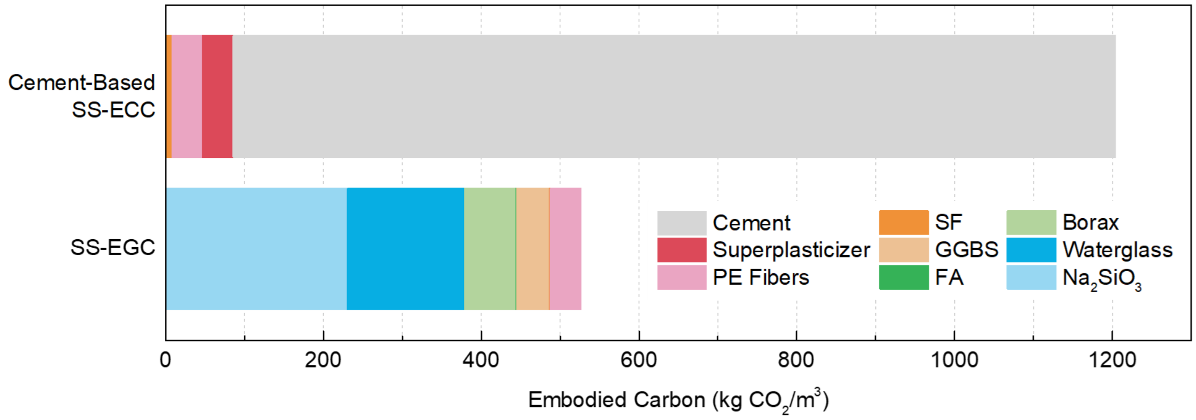

Fig. 17 Embodied carbon of SS-EGC and cement-based SS-ECC. Compared to the cement-based SS-ECC with similar compressive strength, the developed SS-EGC (F2S8-S) showed significantly lower embodied carbon.

Obviously, the embodied carbon of the cement-based SS-ECC (1204.1 kg CO_2/m^3) was significantly higher than that of SS-EGC (526.2 kg CO_2/m^3). The main body of the embodied carbon for the cement-based SS-ECC came from using Portland cement (92.9%), while the other components only contributed 7.1% of the total embodied carbon. It indicated that using the high volume of Portland cement to produce high-strength ECC is not beneficial for construction sustainability. On the other hand, the total embodied carbon of SS-EGC with a similar strength grade was only 43.7% of that of SS-ECC. In detail, precursor materials did not significantly contribute to the carbon dioxide emission (less than 10%). However, the embodied carbon of SS-EGC mainly comes from the alkaline activators (i.e., 43.8% for Na_2SiO_3 and 28.2% for waterglass) and the retarder (12.3%). At the current stage, activators and retarders are important for the successful production of high-strength high-ductility SS-EGC. Since recycled alkaline activators from waste materials have also been tried to produce geopolymer pastes [61], such materials are believed to be used as full or partial replacements of the current commercial activators, which can further reduce embodied carbon of EGC materials in the future.

6 Conclusions

This study has developed seawater sea-sand Engineered Geopolymer Composites (SS-EGC) with high strength and high ductility, and investigated the influence of seawater and sea-sand (compared to freshwater and washed sea-sand) on the matrix properties and tensile performance of EGC. Two fly ash-to-slag ratios [i.e., 8:2 (F8S2 series) and 2:8 (F2S8 series)] were considered in the EGC matrices. Based on the experimental findings, the following conclusions can be drawn.

- Using seawater and sea-sand slightly decreased the compressive strength of EGC (from 89.0 to 84.5 MPa for F8S2 series, and from 145.1 to 143.0 MPa for the F2S8 series), due to the interaction between seawater and alkali activator. It was found that SS-EGC mix showed slightly lower heat releasing rate compared to the freshwater counterpart. The use of seawater increased the fraction of ultra-high-density phase but decreased the fractions of low-density and high-density C-(N)-A-S-H. The ultra-high-density phases in EGC possibly consisted of C-(N)-A-S-H and hydrotalcite, and the content of the latter increased in the seawater-mixed matrix.
- For the tensile performance, using seawater and sea-sand increased the tensile strength but decreased the tensile ductility of EGC. For the cracking behavior, the use of seawater and sea-sand had a marginal effect on the cracking behavior of the F8S2 series, while it decreased both the crack width (from 70.0 to 59.4 μm) and crack width deviation (from 23.4 to 15.7 μm) of F2S8 series. In summary, compared to the F8S2 series, using seawater and sea-sand had a more pronounced effect on the overall performance of the F2S8 series.
- Compared to the cement-based SS-ECC (with similar compressive strength and the same fiber reinforcement) in literature [24], geopolymer-based SS-EGC (F2S8-S) had a similar tensile strain capacity, a higher tensile strength and a superior crack resistance. Notably, the SS-EGC (F2S8-S) showed a significantly lower embodied carbon than the cement-

based SS-ECC. It should be pointed out that owing to the limitation of existing database, more efforts are needed to understand the differences between SS-EGC and cement-based SS-ECC in future studies.

Acknowledgments

The authors would like to acknowledge the financial support received from the Hong Kong Research Grants Council (No. T22-502/18-R), Chinese Guangdong Province R&D Plan for Key Areas (No. 2019B111107002), and The Hong Kong Polytechnic University through the Research Institute for Land and Space (No. CD7D). Jian-Cong Lao and Bo-Tao Huang would like to acknowledge the support by the Hong Kong Innovation and Technology Fund (Project Code: ITS/077/18FX) through the Research Talent Hub.

Declaration of competing interest

The authors declare that they have no known competing financial interests or personal relationships that could have appeared to influence the work reported in this paper.

CRediT Author Statement

JC Lao: Conceptualization, Investigation, Validation, Formal analysis, Writing - Original Draft. **BT Huang**: Conceptualization, Methodology, Visualization, Writing - Original Draft, Writing - Review & Editing. **LY Xu**: Formal analysis, Writing - Review & Editing. **M Khan**: Data acquisition, Validation, Writing - Review & Editing. **Y Fang**: Formal analysis, Writing - Review & Editing. **JG Dai**: Funding Acquisition, Project administration, Supervision, Writing - Review & Editing.

References

1. Li, V. C. (2019). Engineered Cementitious Composites (ECC) - Bendable Concrete for Sustainable and Resilient Infrastructure. Verlag GmbH Germany: Springer, Berlin, Heidelberg.
2. Li, V. C., Wang, S., & Wu, C. (2001). Tensile strain-hardening behavior of polyvinyl alcohol engineered cementitious composite (PVA-ECC). ACI Materials Journal, 98(6), 483-492.
3. Qian, S., Zhou, J., De Rooij, M. R., Schlangen, E., Ye, G., & Van Breugel, K. (2009). Self-healing behavior of strain hardening cementitious composites incorporating local waste materials. Cement and Concrete Composites, 31(9), 613-621.

4. Li, Q. H., Yin, X., Huang, B. T., Luo, A. M., Lyu, Y., Sun, C. J., & Xu, S. L. (2021). Shear interfacial fracture of strain-hardening fiber-reinforced cementitious composites and concrete: A novel approach. Engineering Fracture Mechanics, 253, 107849.

5. Richard, P., & Cheyrezy, M. (1995). Composition of reactive powder concretes. Cement and Concrete Research, 25(7), 1501-1511.

6. Wille, K., Naaman, A. E., El-Tawil, S., & Parra-Montesinos, G. J. (2012). Ultra-high performance concrete and fiber reinforced concrete: achieving strength and ductility without heat curing. Materials and Structures, 45(3), 309-324.

7. Shen, X., & Brühwiler, E. (2020). Influence of local fiber distribution on tensile behavior of strain hardening UHPFRC using NDT and DIC. Cement and Concrete Research, 132, 106042.

8. Huang, B. T., Dai, J. G., Weng, K. F., Zhu, J. X., & Shah, S. P. (2021). Flexural Performance of UHPC–Concrete–ECC Composite Member Reinforced with Perforated Steel Plates. Journal of Structural Engineering, 147(6), 04021065.

9. Li, V. C., & Leung, C. K. Y. (1992). Steady-state and multiple cracking of short random fiber composites. Journal of Engineering Mechanics, 118(11), 2246-2264.

10. Leung, C. K. (1996). Design criteria for pseudoductile fiber-reinforced composites. Journal of Engineering Mechanics, 122(1), 10-18.

11. Xu, L. Y., Huang, B. T., Li, V. C., & Dai, J. G. (2022). High-strength high-ductility Engineered/Strain-Hardening Cementitious Composites (ECC/SHCC) incorporating geopolymer fine aggregates. Cement and Concrete Composites, 125, 104296.

12. Huang, B. T., Zhu, J. X., Weng, K. F., Li, V. C., & Dai, J. G. (2022). Ultra-high-strength engineered/strain-hardening cementitious composites (ECC/SHCC): Material design and effect of fiber hybridization. Cement and Concrete Composites, 129, 104464.

13. Zhu, J. X., Xu, L. Y., Huang, B. T., Weng, K. F., & Dai, J. G. (2022). Recent developments in Engineered/Strain-Hardening Cementitious Composites (ECC/SHCC) with high and ultra-high strength. Construction and Building Materials, 342, 127956.

14. Yoo, D. Y., & Banthia, N. (2022). High-performance strain-hardening cementitious composites with tensile strain capacity exceeding 4%: A review. Cement and Concrete Composites, 125, 104325.

15. Curosu, I., Mechtcherine, V., & Millon, O. (2016). Effect of fiber properties and matrix composition on the tensile behavior of strain-hardening cement-based composites (SHCCs) subject to impact loading. Cement and Concrete Research, 82, 23-35.

16. Chen, Y., Yu, J., & Leung, C. K. (2018). Use of high strength strain-hardening cementitious composites for flexural repair of concrete structures with significant steel corrosion. Construction and Building Materials, 167, 325-337.

17. Huang, B. T., Yu, J., Wu, J. Q., Dai, J. G., & Leung, C. K. (2020). Seawater sea-sand Engineered Cementitious Composites (SS-ECC) for marine and coastal applications. Composites Communications,

20, 100353.

18. Huang, B. T., Weng, K. F., Zhu, J. X., Xiang, Y., Dai, J. G., & Li, V. C. (2021). Engineered/strain-hardening cementitious composites (ECC/SHCC) with an ultra-high compressive strength over 210 MPa. Composites Communications, 26, 100775.
19. Teng, J. G., Xiang, Y., Yu, T., & Fang, Z. (2019). Development and mechanical behaviour of ultra-high-performance seawater sea-sand concrete. Advances in Structural Engineering, 22(14), 3100-3120.
20. Huang, B. T., Wang, Y. T., Wu, J. Q., Yu, J., Dai, J. G., & Leung, C. K. (2021). Effect of fiber content on mechanical performance and cracking characteristics of ultra-high-performance seawater sea-sand concrete (UHP-SSC). Advances in Structural Engineering, 24(6), 1182-1195.
21. Ebead, U., Lau, D., Lollini, F., Nanni, A., Suraneni, P., & Yu, T. (2022). A review of recent advances in the science and technology of seawater-mixed concrete. Cement and Concrete Research, 152, 106666.
22. Zeng, J. J., Liao, J., Zhuge, Y., Guo, Y. C., Zhou, J. K., Huang, Z. H., & Zhang, L. (2022). Bond behavior between GFRP bars and seawater sea-sand fiber-reinforced ultra-high strength concrete. Engineering Structures, 254, 113787.
23. Huang, B. T., Wu, J. Q., Yu, J., Dai, J. G., & Leung, C. K. (2020). High-strength seawater sea-sand Engineered Cementitious Composites (SS-ECC): Mechanical performance and probabilistic modeling. Cement and Concrete Composites, 114, 103740.
24. Huang, B. T., Wu, J. Q., Yu, J., Dai, J. G., Leung, C. K., & Li, V. C. (2021). Seawater sea-sand engineered/strain-hardening cementitious composites (ECC/SHCC): Assessment and modeling of crack characteristics. Cement and Concrete Research, 140, 106292.
25. Provis, J. L. (2018). Alkali-activated materials. Cement and Concrete Research, 114, 40-48.
26. Xu, L. Y., Qian, L. P., Huang, B. T., & Dai, J. G. (2021). Development of artificial one-part geopolymer lightweight aggregates by crushing technique. Journal of Cleaner Production, 315, 128200.
27. Lao, J. C., Xu, L. Y., Huang, B. T., Dai, J. G., & Shah, S. P. (2022). Strain-hardening Ultra-High-Performance Geopolymer Concrete (UHPGC): Matrix design and effect of steel fibers. Composites Communications, 30, 101081.
28. Peng, K. D., Huang, B. T., Xu, L. Y., Hu, R. L., & Dai, J. G. (2022). Flexural strengthening of reinforced concrete beams using geopolymer-bonded small-diameter CFRP bars. Engineering Structures, 256, 113992.
29. Lee, B. Y., Cho, C. G., Lim, H. J., Song, J. K., Yang, K. H., & Li, V. C. (2012). Strain hardening fiber reinforced alkali-activated mortar–a feasibility study. Construction and Building Materials, 37, 15-20.
30. Ohno, M., & Li, V. C. (2014). A feasibility study of strain hardening fiber reinforced fly ash-based geopolymer composites. Construction and Building Materials, 57, 163-168.
31. Nematollahi, B., Sanjayan, J., Qiu, J., & Yang, E. H. (2017). Micromechanics-based investigation of a sustainable ambient temperature cured one-part strain hardening geopolymer composite. Construction and Building Materials, 131, 552-563.

32. Kumar, S., Das, C. S., Lao, J., Alrefaei, Y., & Dai, J. G. (2022). Effect of sand content on bond performance of engineered geopolymer composites (EGC) repair material. Construction and Building Materials, 328, 127080.

33. Yoo, D. Y., Lee, S. K., You, I., Oh, T., Lee, Y., & Zi, G. (2022). Development of strain-hardening geopolymer mortar based on liquid-crystal display (LCD) glass and blast furnace slag. Construction and Building Materials, 331, 127334.

34. Ling, Y., Wang, K., Li, W., Shi, G., & Lu, P. (2019). Effect of slag on the mechanical properties and bond strength of fly ash-based engineered geopolymer composites. Composites Part B: Engineering, 164, 747-757.

35. ASTM C618 – 19. (2019). Standard Specification for Coal Fly Ash and Raw or Calcined Natural Pozzolan for Use in Concrete, ASTM International, West Conshohocken, PA.

36. ASTM C109/C109M. (2013). Standard Test Method for Compressive Strength of Hydraulic Cement Mortars, ASTM International, West Conshohocken, PA.

37. Japan Society of Civil Engineers. (2008), Recommendations for Design and Construction of High Performance Fiber Reinforced Cement Composites with Multiple Fine Cracks (HPFRCC), Concrete Engineering Series No. 82.

38. Ismail, I., Bernal, S. A., Provis, J. L., San Nicolas, R., Hamdan, S., & van Deventer, J. S. (2014). Modification of phase evolution in alkali-activated blast furnace slag by the incorporation of fly ash. Cement and Concrete Composites, 45, 125-135.

39. Shi, D., Yao, Y., Ye, J., & Zhang, W. (2019). Effects of seawater on mechanical properties, mineralogy and microstructure of calcium silicate slag-based alkali-activated materials. Construction and Building Materials, 212, 569-577.

40. Marjanović, N., Komljenović, M., Baščarević, Z., Nikolić, V., & Petrović, R. (2015). Physical–mechanical and microstructural properties of alkali-activated fly ash–blast furnace slag blends. Ceramics International, 41(1), 1421-1435.

41. Ren, J., Sun, H., Cao, K., Ren, Z., Zhou, B., Wu, W., & Xing, F. (2021). Effects of natural seawater mixing on the properties of alkali-activated slag binders. Construction and Building Materials, 294, 123601.

42. Shi, C., & Day, R. L. (1995). A calorimetric study of early hydration of alkali-slag cements. Cement and concrete Research, 25(6), 1333-1346.

43. Kim, M. S., Jun, Y., Lee, C., & Oh, J. E. (2013). Use of CaO as an activator for producing a price-competitive non-cement structural binder using ground granulated blast furnace slag. Cement and concrete research, 54, 208-214.

44. Zhang, S., Li, Z., Ghiassi, B., Yin, S., & Ye, G. (2021). Fracture properties and microstructure formation of hardened alkali-activated slag/fly ash pastes. Cement and Concrete Research, 144, 106447.

45. Jun, Y., Kim, T., & Kim, J. H. (2020). Chloride-bearing characteristics of alkali-activated slag mixed

with seawater: Effect of different salinity levels. Cement and Concrete Composites, 112, 103680.

46. Richardson, I. G., & Li, S. (2018). Composition and structure of an 18-year-old 5M KOH-activated ground granulated blast-furnace slag paste. Construction and Building Materials, 168, 404-411.

47. Islam, M., & Patel, R. (2009). Nitrate sorption by thermally activated Mg/Al chloride hydrotalcite-like compound. Journal of hazardous materials, 169(1-3), 524-531.

48. Kristóf-Makó, É., & Juhász, A. Z. (1999). The effect of mechanical treatment on the crystal structure and thermal decomposition of dolomite. Thermochimica Acta, 342(1-2), 105-114.

49. Hay, R., Li, J., & Celik, K. (2020). Influencing factors on micromechanical properties of calcium (alumino) silicate hydrate C-(A-) SH under nanoindentation experiment. Cement and Concrete Research, 134, 106088.

50. Myers, R. J., L'Hôpital, E., Provis, J. L., & Lothenbach, B. (2015). Effect of temperature and aluminium on calcium (alumino) silicate hydrate chemistry under equilibrium conditions. Cement and Concrete Research, 68, 83-93.

51. Miller, M., Bobko, C., Vandamme, M., & Ulm, F. J. (2008). Surface roughness criteria for cement paste nanoindentation. Cement and Concrete Research, 38(4), 467-476.

52. Oliver, W. C., & Pharr, G. M. (1992). An improved technique for determining hardness and elastic modulus using load and displacement sensing indentation experiments. Journal of materials research, 7(6), 1564-1583.

53. Fang, Y., Wang, J., Qian, X., Wang, L., Chen, P., & Qiao, P. (2022). A renewable admixture to enhance the performance of cement mortars through a pre-hydration method. Journal of Cleaner Production, 332, 130095.

54. Zhang, Y., Liang, M., Gan, Y., & Çopuroğlu, O. (2022). Micro-Mechanical Properties of Slag Rim Formed in Cement–Slag System Evaluated by Nanoindentation Combined with SEM. Materials, 15(18), 6347.

55. Moradi, M., Ashraf, W., & Tian, N. (2022). Monitoring temperature-induced in-situ nanomechanical changes of cement paste by nanoindentation. MRS Advances, 7(10), 217-221.

56. Aveston, J., Mercer, R. A., & Siltwood, J. M. (1974). Fiber reinforced cements—scientific foundations for specifications. Composites standards testing arid design, Conference Proceedings National Physical Laboratory, IPC Science and Technology Press, Guildford, United Kingdom, 93-103.

57. Li, V. C. (1992). Postcrack scaling relations for fiber reinforced cementitious composites. Journal of Materials in Civil Engineering, 4(1), 41-57.

58. Liu, W. H., Zhang, L. W., & Liew, K. M. (2020). Modeling of crack bridging and failure in heterogeneous composite materials: A damage-plastic multiphase model. Journal of the Mechanics and Physics of Solids, 143, 104072.

59. Sonat, C., He, S., Li, J., Unluer, C., & Yang, E. H. (2021). Strain hardening magnesium-silicate-hydrate composites (SHMSHC) reinforced with short and randomly oriented polyvinyl alcohol microfibers.

Cement and Concrete Research, 142, 106354.

60. Xu, M., Song, S., Feng, L., Zhou, J., Li, H., & Li, V. C. (2021). Development of basalt fiber engineered cementitious composites and its mechanical properties. Construction and Building Materials, 266, 121173.

61. Alnahhal, M. F., Kim, T., & Hajimohammadi, A. (2021). Waste-derived activators for alkali-activated materials: A review. Cement and Concrete Composites, 118, 103980.

62. Hammond, G. P., & Jones, C. I. (2008). Embodied energy and carbon in construction materials. Proceedings of the Institution of Civil Engineers-Energy, 161(2), 87-98.

63. Vijayarethinam, N. (2009). Silica fume applications. World Cement, 40, 97-100.

64. Shoji, D., He, Z., Zhang, D., & Li, V. C. (2022). The greening of engineered cementitious composites (ECC): A review. Construction and Building Materials, 327, 126701.

65. Yu, J., Chen, Y., & Leung, C. K. (2019). Mechanical performance of Strain-Hardening Cementitious Composites (SHCC) with hybrid polyvinyl alcohol and steel fibers. Composite Structures, 226, 111198.

66. Yang, T., Zhang, Z., Zhang, F., Gao, Y., & Wu, Q. (2020). Chloride and heavy metal binding capacities of hydrotalcite-like phases formed in greener one-part sodium carbonate-activated slag cements. Journal of Cleaner Production, 253, 120047.

67. Pasupathy, K., Ramakrishnan, S., & Sanjayan, J. (2023). 3D concrete printing of eco-friendly geopolymer containing brick waste. Cement and Concrete Composites, 104943.

68. Zhang, D., Yu, J., Wu, H., Jaworska, B., Ellis, B. R., & Li, V. C. (2020). Discontinuous micro-fibers as intrinsic reinforcement for ductile Engineered Cementitious Composites (ECC). Composites Part B: Engineering, 184, 107741.

69. Xu, L. Y., Huang, B. T., Lan-Ping, Q., & Dai, J. G. (2022). Enhancing long-term tensile performance of Engineered Cementitious Composites (ECC) using sustainable artificial geopolymer aggregates. Cement and Concrete Composites, 133, 104676.

70. Song, Y., Li, Z., Zhang, J., Tang, Y., Ge, Y., & Cui, X. (2020). A low-cost biomimetic heterostructured multilayer membrane with geopolymer microparticles for broad-spectrum water purification. ACS Applied Materials & Interfaces, 12(10), 12133-12142.